



# PEMFC-Performance of Unsupported Pt-Ni Aerogel Cathode Catalyst Layers under Automotive-Relevant Operative Conditions

Meriem Fikry,<sup>1</sup>  Juan Herranz,<sup>1,z</sup>  Simon Leisibach,<sup>1</sup> Pavel Khavlyuk,<sup>2</sup> Alexander Eychmüller,<sup>2</sup> and Thomas J. Schmidt<sup>1,3</sup>

<sup>1</sup>Electrochemistry Laboratory, Paul Scherrer Institut, 5232 Villigen/Switzerland

<sup>2</sup>Physical Chemistry, Technische Universität Dresden, 01062 Dresden/Germany

<sup>3</sup>Institute for Molecular Physical Science, ETH Zürich, 8093 Zürich/Switzerland

Unsupported, Pt-based electrocatalysts hold great potential for implementation in polymer electrolyte membrane fuel cell (PEMFC-) cathodes owing to their enhanced durability under startup/shutdown conditions entailing high potential excursions. Among such materials, the recently developed Pt-Ni aerogel consisting of tridimensional nanochains of interconnected nanoparticles has already been shown to feature an initial PEMFC-performance comparable to that of C-supported Pt-nanoparticles (Pt/C) along with a much better startup/shutdown durability. However, all PEMFC characterization of this materials has been carried out at 80 °C and using fully humidified gases, and its behavior under more demanding conditions concomitant to its potential implementation for automotive applications remains unexplored. Thus, in this work aerogel catalyst layers (CLs) are characterized under a wide range of temperatures and relative humidities, as well as submitted to fast current up-transients. These extensive tests showed that the performance of the aerogel CLs is comparable to that of a commercial Pt/C benchmark, except at high current densities and low temperatures at which the thin aerogel layers suffer from a low water storage capacity.

© 2023 The Author(s). Published on behalf of The Electrochemical Society by IOP Publishing Limited. This is an open access article distributed under the terms of the Creative Commons Attribution 4.0 License (CC BY, <http://creativecommons.org/licenses/by/4.0/>), which permits unrestricted reuse of the work in any medium, provided the original work is properly cited. [DOI: 10.1149/1945-7111/ad0e45]



Manuscript submitted August 14, 2023; revised manuscript received November 8, 2023. Published November 29, 2023.

Supplementary material for this article is available [online](#)

The extensive commercialization of polymer electrolyte membrane fuel cells (PEMFCs) relies on the utilization of carbon supported Pt-based catalyst (Pt/C) to speed up the hydrogen oxidation and oxygen reduction reactions (HOR, ORR) in each cell's anode and cathode, respectively. The high Pt loading (typically  $\approx 0.4 \text{ mg}_{\text{Pt}} \cdot \text{cm}^{-2}$ ) required by the sluggish ORR-kinetics dictates a major part of the PEMFC-stack costs, of which  $\approx 40\%$  are expected to stem from these catalysts once a manufacturing a volume of  $\geq 500,000$  units/annum will be reached (assuming passenger vehicle stacks with a nominal power output of  $80 \text{ kW}_{\text{net}}/\text{unit}$ ).<sup>1,2</sup> In addition to this cost argument, device durability is also insufficient, in part due to the carbon supports used in commercial Pt/C catalyst in both anode<sup>3</sup> and cathode sides.<sup>4</sup> Specifically, these C-supports can suffer from severe corrosion upon start-up/shut down events if the latter result in high cathode potentials ( $> 1.5 \text{ V}$  vs the reversible hydrogen electrode ( $V_{\text{RHE}}$ )) that cause Pt-nanoparticle detachment, massive ECSA loss, cathode thinning and a fast degradation of the PEMFC performance over time.<sup>5</sup> Therefore, in order to reach the ultimate cost and durability performance targets of  $\leq \text{US\$ } 30/\text{kW}_{\text{net,stack}}$  and  $\geq 8000 \text{ h}$ <sup>6,7</sup> of on-road operation set by the U.S. Department of Energy (DOE), respectively, the Pt-loading should be reduced and the durability enhanced.

To tackle both of these challenges, in a previous work Henning et al.<sup>8</sup> developed a novel bimetallic and carbon-free catalyst consisting of tridimensionally-interconnected Pt-nanoparticles alloyed with Ni, and referred to as "aerogel." This material displayed a  $\approx 2.5$ -fold greater surface-specific-ORR activity than a commercial Pt/C catalyst at standard PEMFC-conditions, namely at a cell temperature of 80 °C, 100% relative humidity (RH) and an  $\text{O}_2$ -pressure of 1.50 bar<sub>abs</sub>.<sup>8</sup> Furthermore, when this same Pt-Ni aerogel was submitted to an accelerated test stress (AST) that mimics PEMFC startup/shutdown, it preserved  $\approx 90\%$  of its initial ORR-performance (as compared to only  $\approx 40\%$  for a commercial Pt/C benchmark exposed to the same AST).<sup>4</sup> The aerogel catalyst layers (CLs) in that work<sup>4</sup> (with a Pt-loading of  $\approx 0.3 \text{ mg}_{\text{Pt}} \cdot \text{cm}^{-2}$ ) were prepared by implementing a pore inducer in the catalyst ink formulation that increased the CL-porosity and shifted the pore sizes

towards the mesoporous range (i.e., to diameters  $> 50 \text{ nm}$ ).<sup>8</sup> However, those same inks were processed into catalyst coated membranes (CCMs) by hand-spraying which, as we have recently shown,<sup>9</sup> is highly dependent on the operator and leads to irreproducibility issues. Thus, in attempt to overcome this irreproducibility, we recently adapted the CCM-processing methods to the use of an automated spray-coating machine that yielded homogenous and highly porous aerogel CLs without the need for a pore inducer, and that featured the same PEMFC-performance as those manufactured by Henning and coworkers.<sup>9</sup>

Beyond this progress in the upscaling of aerogel synthesis and CCM- manufacture, to this date these Pt-Ni aerogel CLs have only been characterized under standard PEMFC-conditions (namely, at 80 °C, 100% RH and 1.50 bar<sub>abs</sub>). However, to fully illustrate this catalyst's applicability in the specific context of automotive applications, their performance has to be characterized under a broader range of operative states. To this end, in the present work we carried out a complete electrochemical characterization of the PEMFC-performance of the Pt-Ni aerogel at temperatures  $\leq 80 \text{ °C}$  and RHs  $\leq 100\%$ , as well as upon fast transients from low to high current densities. This behavior was systematically benchmarked against a commercial Pt/C CL and discussed at length in the specific context of the large difference between both materials' CL-thicknesses and corresponding void volumes.

## Experimental

**Synthesis.**—The up-scaled synthesis of the Pt-Ni aerogel used in this work was described in detail in our recent publication.<sup>9</sup> In few words, 2.925 ml of a 0.205 M  $\text{H}_2\text{PtCl}_6$  solution (8 wt % in  $\text{H}_2\text{O}$ , Sigma Aldrich) and 20 ml of a freshly prepared 10 mM  $\text{NiCl}_2$  solution ( $\text{NiCl}_2 \cdot 6\text{H}_2\text{O}$ , 99%, Sigma Aldrich) were dissolved in 4000 ml of ultrapure water ( $18.2 \text{ M}\Omega \cdot \text{cm}$ , Millipore) and stirred until the mixing was complete. Subsequently, 35 ml of a freshly prepared 0.1 M  $\text{NaBH}_4$  solution (granular, 99.99%, Sigma Aldrich) were added while stirring vigorously. The resulting brown solution was kept stirring for another 30 min. Later, the reaction solution was left at a temperature of 60 °C for one day of gelation. As a result, a black Pt-Ni hydrogel formed at the bottom of the container, and was first washed with water and then solvent-exchanged with *tert*-

<sup>z</sup>E-mail: [juan.herranz@psi.ch](mailto:juan.herranz@psi.ch)

butanol ( $\geq 99.5\%$ , Thermo Scientific). The obtained anhydrous gels were exposed to freeze drying in a Toption, TOPT-12CS device for 24 h at  $\approx 1$  Pa and at  $-50^\circ\text{C}$ , which yielded  $\approx 125$  mg of the final aerogel material.

**Materials.**—For the fabrication of Pt-Ni aerogel cathodes, catalyst inks of this material were processed similarly to what was described in our recent work.<sup>9</sup> In brief, 13 mg of catalyst powder was dispersed in 5.20 ml of a 95:5 volume mixture of absolute ethanol (EtOH – for HPLC, Sigma Aldrich,  $\geq 99.8\%$ ) and ultra-pure water ( $18.2\text{ M}\Omega\cdot\text{cm}$  ELGA Purelab Ultra). Subsequently, the required amount of Dupont's Nafion D2020 ionomer suspension needed to yield an ionomer-to-catalyst (I/C) mass ratio of 0.12 was added.<sup>8</sup> The resulting ink was sonicated (USC100T, 45 kHz, VWR) for 20 min and sprayed onto a pre-cut piece of Nafion HP membrane (Ion Power) confined in a holder exposing an active area of  $1\text{ cm}^2$ . This spraying was carried out using an automated spray-coating system (Sono-Tek) equipped with a 25 kHz ultrasonic acoustic nozzle, and resulted in homogenous catalyst coated membranes (CCMs). The latter had a targeted cathode catalyst loadings of  $0.3\text{ mg}_{\text{Pt}}\cdot\text{cm}^{-2}$ , which was verified on an individual CCM basis by weighing the membrane before and after spraying using a dummy membrane to account for deviations in the base weight caused by variations in the room's RH.<sup>10</sup>

**MEA preparation and conditioning.**—Membrane electrode assemblies (MEAs) with an active area of  $1\text{ cm}^2$  were fabricated in house by hot pressing the aerogel-based CCM described above at  $120^\circ\text{C}$  and 1 bar for 5 min. The CCM was previously sandwiched between a Sigracet 29BC gas diffusion layer (GDL) in the cathode side and a commercial GDE (acquired from Johnson Matthey) made of a SGL 29 BC GDL with microporous layer (MPL) and a Pt/C catalyst layer (CL) with a Pt-loading of  $0.4\text{ mg}_{\text{Pt}}\cdot\text{cm}^{-2}$  (HISPEC 9100) in the anode side. The Pt/C electrodes used for cathode performance benchmarking were cut from the same commercial GDE and were hot pressed at equivalent conditions in both anode and cathode sides, again sandwiched between a piece of Nafion HP membrane.

All PEMFC electrochemical measurements in this work were performed in a differential cell developed in house and containing 5 channels of 1 mm in width forming an active area of  $1\text{ cm}^2$ .<sup>11,12</sup> The use of such differential cell allows studying the MEA under homogenous well-defined conditions, in the absence of along the channel effects, such as changing in temperature, relative humidity (RH) and gas concentration.<sup>8,11</sup> Prior to each PEMFC test, the differential cell was assembled by placing the MEA between two polytetrafluoroethylene (PTFE) gaskets (at the anode and cathode sides) to seal the MEA between the flow fields and avoid any gas leakage. The compression was adjusted to  $\approx 25\%$  (assuming that the MPLs and CLs are incompressible) by stacking steel spacers of defined thicknesses, and the cell was assembled with a final torque of 60 N·m.<sup>11,12</sup> All fuel cell tests were performed in an in house test station and using a Biologic VSP-300 potentiostat with a 10 A/5 V

current booster. Prior to any electrochemical characterization, all MEAs were conditioned in a voltage-controlled break-in procedure at  $80^\circ\text{C}$ , 100% RH and 1.70 bar<sub>abs</sub> with  $600\text{ nml}\cdot\text{min}^{-1}$  of  $\text{H}_2$  flow and  $1350\text{ nml}\cdot\text{min}^{-2}$  of air at anode and cathode, respectively. Specifically, the voltage sequence consisted of 8 cycles implying (i) 45 min at 0.6 V, (ii) 5 min at 0.95 V, and (iii) 10 min at 0.85 V.<sup>13</sup> Finally the cell was cooled down and further electrochemical diagnostics were performed (*vide infra*).

**In situ fuel cell electrochemical diagnostics.**—Prior to any PEMFC testing at temperatures  $< 80^\circ\text{C}$  or RHs  $< 100\%$ , a first electrochemical characterization was performed at standard conditions, namely at  $80^\circ\text{C}$ , 100% RH and 1.70 bar<sub>abs</sub> in order to verify that the baseline PEMFC performance agrees with our previous measurements using these same materials under such conditions.<sup>8,9</sup>

At the beginning-of-life and after the break-in protocol, cyclic voltammograms (CVs) were recorded at room temperature, ambient pressure and 100% RH. For this, the cathode potential was scanned between 0.06 and 1.0 V at  $50\text{ mV}\cdot\text{s}^{-1}$  with the anode (which acted as a counter/reference electrode) fed with a  $\text{H}_2$  flow rate of  $100\text{ nml}\cdot\text{min}^{-1}$  and the  $\text{N}_2$ -flow at the cathode halted just prior to the measurement. The cathodic electrochemical surface area (ECSA) was calculated from the CV recorded after the break-in procedure and cool down of the cell. The ECSA values were averaged from the H-adsorption and -desorption charges between 0.08 and 0.4 V<sub>RHE</sub> after double-layer correction, assuming a conversion factor of  $210\text{ }\mu\text{C}\cdot\text{cm}_{\text{Pt}}^{-2}$ .<sup>14,15</sup>

The ohmic short of the membrane and the  $\text{H}_2$ -crossover were determined via linear sweep voltammetry (LSV) from 0.6 to 0.1 V<sub>RHE</sub> to obtain the  $\text{H}_2$ -oxidation limiting current before and after the break-in procedure. The measurement was performed at standard conditions, namely at  $80^\circ\text{C}$ , 100% RH and 1.70 bar<sub>abs</sub> in  $\text{H}_2/\text{N}_2$  ( $600/1350\text{ nml}\cdot\text{min}^{-1}$  in the anode and cathode, respectively). In order to minimize the contribution of double layer capacitance and H-adsorption to the measured current, this LSV was recorded at a scan rate of  $1\text{ mV}\cdot\text{s}^{-1}$ .<sup>14</sup> The  $\text{H}_2$ -crossover current densities typically amounted to  $\approx 2.5\text{ mA}\cdot\text{cm}^{-2}_{\text{MEA}}$ .

The proton conduction resistance in the cathode catalyst layer ( $R_{\text{H}^+, \text{cathode}}$ ) was determined by potentiostatic electrochemical impedance spectroscopy (PEIS) with  $600\text{ nml}\cdot\text{min}^{-1}$  of  $\text{H}_2$  in the anode and  $1350\text{ nml}\cdot\text{min}^{-1}$  of  $\text{N}_2$  flow in the cathode at the above standard conditions of  $80^\circ\text{C}$ , 1.70 bar<sub>abs</sub> and 100% RH. The measurement was performed at 0.2 V<sub>RHE</sub> with a voltage perturbation of 1 mV between 500 MHz and 6 mHz (6 points per decade).<sup>16–18</sup>

Polarization curves were recorded with fully humidified gasses in  $\text{H}_2/\text{O}_2$  and  $\text{H}_2/\text{air}$  at 100% RH,  $80^\circ\text{C}$  and 1.70 bar<sub>abs</sub> in a current controlled mode ranging from low to high current densities (5 to  $1500\text{ mA}\cdot\text{cm}^{-2}$ ). The cell current was stabilized for 3 min at each value and the resulting potential was averaged over the last 2 min of each current hold. In parallel, galvanostatic electrochemical impedance spectroscopy (GEIS) measurements were performed in the frequency range from 1 MHz to 200 mHz (with a current perturbation of  $5\text{ mA}\cdot\text{cm}^{-2}$ ) to extract the high frequency resistance (HFR) from the x-axis of the corresponding Nyquist plots.

**Effect of relative humidity.**—To study the effect of relative humidity on Pt-Ni aerogel and benchmark Pt/C CLs polarization curves were recorded as described above at various relative humidities that were varied in two modes: firstly, starting from high to low relative humidity (RH\_1) and secondly going from low to high relative humidity (RH\_2), as shown in Table I. For each material, three different MEAs were tested for each RH-mode, and the resulting performances were then averaged over the three MEAs, so that all reported potential vs current values correspond to the averages over these three measurements and the error bars to their standard deviations. The cell temperature in these measurements at different RHs was systematically maintained at  $80^\circ\text{C}$  and the pressure of 1.70 bar<sub>abs</sub>, and the current vs potential curves were

**Table I. Experimental parameters applied for the measurements at varying relative humidities, whereby the chronology of each measurement mode is set in the order from the top to the bottom values of each corresponding column.**

RH_1 [%]	RH_2 [%]	Temperature [ $^\circ\text{C}$ ]	Pressure [bar <sub>abs</sub> ]
100	40	80	1.70
90	50		
80	60		
70	70		
60	80		
50	90		
40	100		

**Table II.** Experimental parameters applied for the measurements at varying temperatures, whereby the chronology of each measurement mode is set in the order from the top to the bottom values of each corresponding column.

T <sub>1</sub> [°C]	T <sub>2</sub> [°C]	RH [%]	Pressure [bar <sub>abs</sub> ]
80	40	100	1.70
	50		
60	60		
	70		
40	80		

recorded in H<sub>2</sub>: air as described above. Additionally, PEIS-spectra were also recorded as previously described at each relative humidity to analyze the effect of this variable on the proton conduction resistance of the cathode catalyst layer.

**Effect of temperature.**—To assess the effect of temperature on the performance of the Pt-Ni aerogel and Pt/C CLs, the relative humidity was kept constant at 100% and the temperature was varied in two different modes, similarly to what was described above for the RH-study. Namely, in the T<sub>1</sub> mode, the temperature was modified from a high to a low value (i.e., from 80 to 40 °C, in 20 °C increments), while in the T<sub>2</sub> mode it was increased from 40 to 80 °C in 10 °C steps (see Table II). At each temperature, polarization curves in H<sub>2</sub>: air and impedance spectra in H<sub>2</sub>:N<sub>2</sub> were recorded at 100% RH and 1.70 bar<sub>abs</sub>. Three different MEAs of each material (i.e., Pt-Ni aerogel and Pt/C) were studied for each temperature case and their performances were again averaged for the values reported in what follows (whereby error bars correspond to standard deviations).

**Up-transient tests.**—The load transient experiments were performed under different relative humidity and temperature conditions. The gas flows were maintained at 600 vs 1350 nml·min<sup>-1</sup> of H<sub>2</sub> vs air at anode vs cathode, respectively, while the pressure was held constant at 1.70 bar<sub>abs</sub>. The cell voltage was first set to 0.6 V for 10 min, and then the current was reduced to 0.02 A·cm<sup>-2</sup> for 2 min. Finally, the current was ramped up to 1 A·cm<sup>-2</sup> within 1 s.<sup>19</sup> Figure S1 shows a typical up-transient test with the current change and the voltage response. If the voltage responses is <0, the test is considered as failed due to excessive water accumulation (i.e., flooding) in the cathode catalyst layer.

**Mass transport overpotential determination.**—The measured PEMFC potential ( $E_{\text{cell}}$ ) is a result of different overpotential contributions summarized in Eq. 1, which describes the terms associated with the cathodic reaction based on the assumption that the hydrogen oxidation reaction (HOR-) kinetics and H<sup>+</sup> conduction overpotentials at the anode CL are negligible:<sup>20</sup>

$$E_{\text{cell}} = E_{\text{rev}} - \eta_{\text{ORR}} - \eta_{\text{HFR}} - \eta_{\text{H}^+, \text{cathode}}^{\text{eff}} - \eta_{\text{tx}} \quad [1]$$

where  $E_{\text{rev}}$  is the equilibrium thermodynamic potential, which is dependent on the gasses partial pressures and the operating temperature;<sup>21</sup>  $\eta_{\text{ORR}}$  is the cathodic oxygen reduction reaction (ORR) overpotential;  $\eta_{\text{HFR}}$  is the ohmic overpotential given by  $i$ -HFR, where  $i$  is the current density and HFR is the ohmic resistance corresponding to the intercept of the Nyquist plot with the imaginary axis (or high frequency resistance, HFR – see Fig. S2 in the SI); and  $\eta_{\text{tx}}$  corresponds to the mass transport overpotential due to O<sub>2</sub> transport resistances through the cathode electrode. Finally, Fig. S3 features an exemplary Nyquist plot recorded on a Pt/C electrode, and displaying a 45° line between 0.04 <Re(Z) <0.06 Ω cm<sup>2</sup> from which the HFR and the  $R_{\text{H}^+, \text{cathode}}$  can be derived. After quantification of  $R_{\text{H}^+, \text{cathode}}$  for both Pt/C and Pt-Ni,

the effective proton resistance ( $R_{\text{H}^+, \text{cathode}}^{\text{eff}}$ ) can be determined via the following equation

$$R_{\text{H}^+, \text{cathode}}^{\text{eff}} = \frac{R_{\text{H}^+, \text{cathode}}}{3 + \zeta} \quad [2]$$

where  $\zeta$  is a dimensionless correction factor that takes into account the cathode utilization and depends on the product of the current density and the  $R_{\text{H}^+, \text{cathode}}$  divided by the ORR-Tafel slope, as explained by Neyerlin et al. and Liu et al.<sup>16,17</sup> In this work, a specific Tafel slope for each given relative humidity and/or temperature was used to obtain the final effective proton resistance through the catalyst layer  $R_{\text{H}^+, \text{cathode}}^{\text{eff}}$ . Finally, the proton resistance overpotential of the cathode CL is determined by multiplying each specific current density by this effective proton transfer resistance (i.e., as  $i \cdot R_{\text{H}^+, \text{cathode}}^{\text{eff}}$ ).

After quantifying these parameters, the cell potential was corrected for the HFR and for  $R_{\text{H}^+, \text{cathode}}^{\text{eff}}$ , and the current density was corrected for the H<sub>2</sub>-crossover (*vide supra*) and for the hydrogen and oxygen partial pressures ( $p_{\text{H}_2}$ ,  $p_{\text{O}_2}$ ) using the equation:<sup>22</sup>

$$i_{p(\text{O}_2, \text{H}_2)}|_{\text{HFR-free}} = i_{\text{Air}} \cdot \left( \frac{p_{\text{O}_2}}{p_{\text{O}_2}^*} \right)^m \cdot \left( \frac{p_{\text{H}_2}}{p_{\text{H}_2}^*} \right)^{\alpha/2} \quad [3]$$

where the references pressures are  $p_{\text{H}_2}^* = p_{\text{O}_2}^* = 1.01$  bar<sub>abs</sub>,  $\alpha$  is transfer coefficient (with an assumed value of 1)<sup>22</sup> and  $m$  is the reaction order with respect to the O<sub>2</sub>-pressure at constant potential with an assumed value of 0.79.<sup>22</sup>

Finally, the currents were also normalized by the catalysts' ECSAs to yield the surface-specific ORR-activity values for each material. The mass transport overpotential was estimated by subtracting the measured voltage from the kinetically-controlled potential that one would expect at a given current density, which was in turn quantified by extending the Tafel line (with a given slope determined by the operative relative humidity and temperature) beyond the purely kinetic regime in which the potential is linearly proportional to the logarithm of the current.

**Pt-oxide coverage determination.**—The Pt oxide coverage at a given potential was determined from the cyclic voltammograms recorded between 0.06 and 1 V at 80 °C, 1.70 bar<sub>abs</sub> and at the different relative humidity values listed in above Table I. Due to the lack of carbon support and reduced thickness of the Pt-Ni aerogel, its capacitive current is very low with regard to that of the Pt/C electrodes, and this leads to a larger contribution of H<sub>2</sub> crossover currents to the so-recorded CVs. Therefore, 5% H<sub>2</sub>-in-argon (Messer, 5.0) was fed to the anode for these aerogel measurements. Besides of this difference, the N<sub>2</sub> cathode gas flow was systematically stopped just prior to the measurements for both material types. In order to accurately reference the cathode potential to a unique H<sub>2</sub>-pressure (using a reference value of  $p_{\text{H}_2}^* = 1.01$  bar<sub>abs</sub>), the H<sub>2</sub> partial pressure was varied with relative humidity, to account for the potential shift associated to the difference in  $p_{\text{H}_2}$  at the anode, as described by the following Nernst equation<sup>23,24</sup>

$$E(p_{\text{H}_2}^*) = E(p_{\text{H}_2}) + \frac{2.303RT}{2F} \log \left( \frac{p_{\text{H}_2}}{p_{\text{H}_2}^*} \right) \quad [4]$$

where  $E(p_{\text{H}_2}^*)$  is the corrected potential at a reference hydrogen pressure ( $p_{\text{H}_2}^*$ ) of 1.01 bar<sub>abs</sub> and  $E(p_{\text{H}_2})$  is the potential at the operative  $p_{\text{H}_2}$  at which the CV measurement was performed.

After correction of the potential ( $E(p_{\text{H}_2}^*)$ ), the Pt-oxide coverage was determined by dividing each incremental charge (10 mV increment) under the Pt-oxide region (0.5 V <  $Q_{\text{ox}}$  < 1 V), by the charge under the H<sup>+</sup> adsorption region (0.05 V <  $Q_{\text{H}^+}$  < 0.5 V), assuming one electron transfer per Pt atom using Eqs. 5 and 6, respectively.<sup>24,25</sup>



$$Q_o = \frac{1}{dV/dt} \int_{0.5V}^{1V} i_{cc} \cdot dV \quad [5]$$

$$Q_{H^+} = \frac{1}{dV/dt} \int_{0.05V}^{0.5V} i_{cc} \cdot dV \quad [6]$$

where  $dV/dt$  is the scan rate and  $i_{cc}$  is the capacitive corrected current.

## Results and Discussion

Prior to presenting the experimental results acquired on the Pt-Ni aerogel and Pt/C cathodes, we highlight the substantial differences between these materials' CLs, which appear summarized in Table III. Specifically, the layers' total thicknesses and porosities were derived from focused ion beam scanning electron microscopy (FIB-SEM) measurements reported in our recent publication.<sup>9</sup> Notably, the Pt-Ni aerogel CL has a  $\approx 6$ -fold lower thickness than the Pt/C layer (due to the concurrent,  $\approx 10$ -fold higher density of the Pt in the aerogel vs the C-support in Pt/C) that may result in insufficient void volume to store liquid water produced at low temperatures or high current densities<sup>19</sup>—the precise effects that we intend to address in this study and that are discussed in the following paragraphs.

**Effect of relative humidity on the CLs' performance.**—To start our experimental study, Fig. 1a showcases the cell performance of both Pt-Ni aerogel and Pt/C CLs in  $H_2$ : air at the two most extreme relative humidities of 100 and 40% used in these measurements and recorded by going from 100 to 40% RH (i.e., in the RH\_1 mode in Table I). Note that the complementing polarization curves and Tafel plots at all intermediate RHs can be found in the supplementary information (cf Figs. S4 and S5). The overall polarization curves are very similar for both materials and RHs, with the decrease in the relative humidity causing a drop of the cell voltage at high current densities that is further discussed below on the basis of a careful overpotential deconvolution featured in Fig. 2. Complementarily, Fig. 1c displays a comparison of the differences among the polarization curves recorded by going from 100 to 40% RH and vice versa (i.e., in the RH\_1 vs RH\_2 modes, respectively), in this case only for the Pt-Ni aerogel. These polarization curves appear to be insensitive to the acquisition mode, and again feature a poorer performance at high current densities in dry conditions.

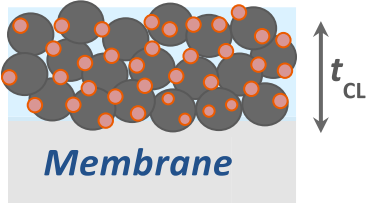

More significant differences among the materials and measurement modes can be identified when assessing in detail the kinetic performances, illustrated by the Tafel plots in Figs. 1b and 1d. Starting with the comparison among Pt-Ni aerogel and Pt/C in the RH\_1 mode in Fig. 1b, it can be noted that the kinetic performance of the aerogel at potentials  $\geq 0.85$  V declines with the decrease of the relative humidity, whereas in the case of Pt/C it improves slightly.

Interestingly, this deterioration of the aerogel's ORR-kinetics at low RHs is less apparent when the polarization curves are recorded starting from 40 and going up to 100% RH (i.e., in the RH\_2 mode). These differences are better visualized by comparing the currents at 0.9 V summarized in Fig. 2a, in which the aerogel's ORR kinetic performance at 40 vs 100% RH is  $\approx 60$  vs  $\approx 20\%$  lower for the RH\_1 vs RH\_2 modes, respectively. By comparison, this acquisition mode has a negligible effect on the ORR-kinetics of the Pt/C CLs, which essentially remain constant over the various RHs applied in these tests. Notably, energy-dispersive X-ray spectroscopy measurements of the end-of-test catalyst layers showed that these retained their Ni-content, and thus the leaching of this non-noble component cannot be the cause for these protocol-specific activity differences. Instead, we hypothesize that this sensitivity of the aerogels' ORR-activity to the measurement mode may be caused by an effect of these protocols on the alloys' strain, which has been tied to this material's ORR performance.<sup>4,26,27</sup>

Beyond these differences, when the higher values of the surface-specific ORR-kinetic currents at 80 °C and  $p_{O_2} = p_{H_2} = 1.01$  bar<sub>abs</sub> are considered (cf Fig. 2a), the Pt-Ni aerogel features a  $\approx 2.5$  fold-higher performance at 0.9 V than Pt/C ( $\approx 280$  vs  $\approx 100 \mu A cm^{-2}_{Pt}$ , respectively), which is consistent with our previous works.<sup>8,9</sup> Most importantly for the overpotential deconvolution presented below, when these ORR-activity values are based on currents normalized with regard to the electrodes' geometric areas (see Fig. S6 in the supplementary information), the two catalysts feature essentially identical kinetic performances at the higher RH of 100%. At 40% RH, though, this ORR performance becomes  $\approx 2$ -fold higher for Pt/C vs the Pt-Ni aerogel. This difference translates into a  $\approx 17$  mV lower kinetic overpotential for the former material (see Fig. S7), which is relevant for the overpotential deconvolution discussed in detail below.

Moving on to the overpotential associated to the transport of protons through the CLs, determined through PEIS measurements, at 100% RH the Pt/C CL possesses an  $R_{H^+,cathode}$  of  $\approx 20 m\Omega cm^2$  (see Fig. 2b) that is in accordance with previous literature,<sup>8,17</sup> while the Pt-Ni aerogel displays a quasi-negligible,  $\approx 20$  times lower  $R_{H^+,cathode}$  value attributable to its CL's reduced thickness ( $\approx 1.5 \mu m$ —*vide supra*).<sup>8,9,28</sup> This behavior is again consistent with our previous observations<sup>8,9</sup> and was also reported for another sort of unsupported catalyst consisting of hollow Pt-Fe nanospheres for which the corresponding CLs feature a thickness within the same order of magnitude as that of our aerogel layers.<sup>29</sup> Moreover, decreasing the relative humidity causes a significant increase in  $R_{H^+,cathode}$  for the Pt/C CLs (with the value of this variable increasing from 20 to  $160 m\Omega \cdot cm^{-2}$  upon lowering the RH from 100 to 40% RH, both for the RH\_1 and RH\_2 modes). On the other hand, the Pt-Ni aerogel CLs still showcase a close-to-negligible proton transport resistance that only increases to  $\approx 5 m\Omega \cdot cm^{-2}$  at 40% RH, thus systematically remaining significantly below the values observed for the Pt/C catalyst layer<sup>17</sup> even at the highest

**Table III.** Graphical representation of the benchmark Pt/C and Pt-Ni aerogel CLs, along with their corresponding porosities and thicknesses derived from FIB-SEM measurements.<sup>9</sup>

	Pt/C	Pt-Ni Aerogel
		
Pt loading [ $mg_{Pt} \cdot cm^{-2}$ ]	0.4	0.3
Porosity [%]	78	75
CL-thickness, $t_{CL}$ [ $\mu m$ ]	10.4	1.7

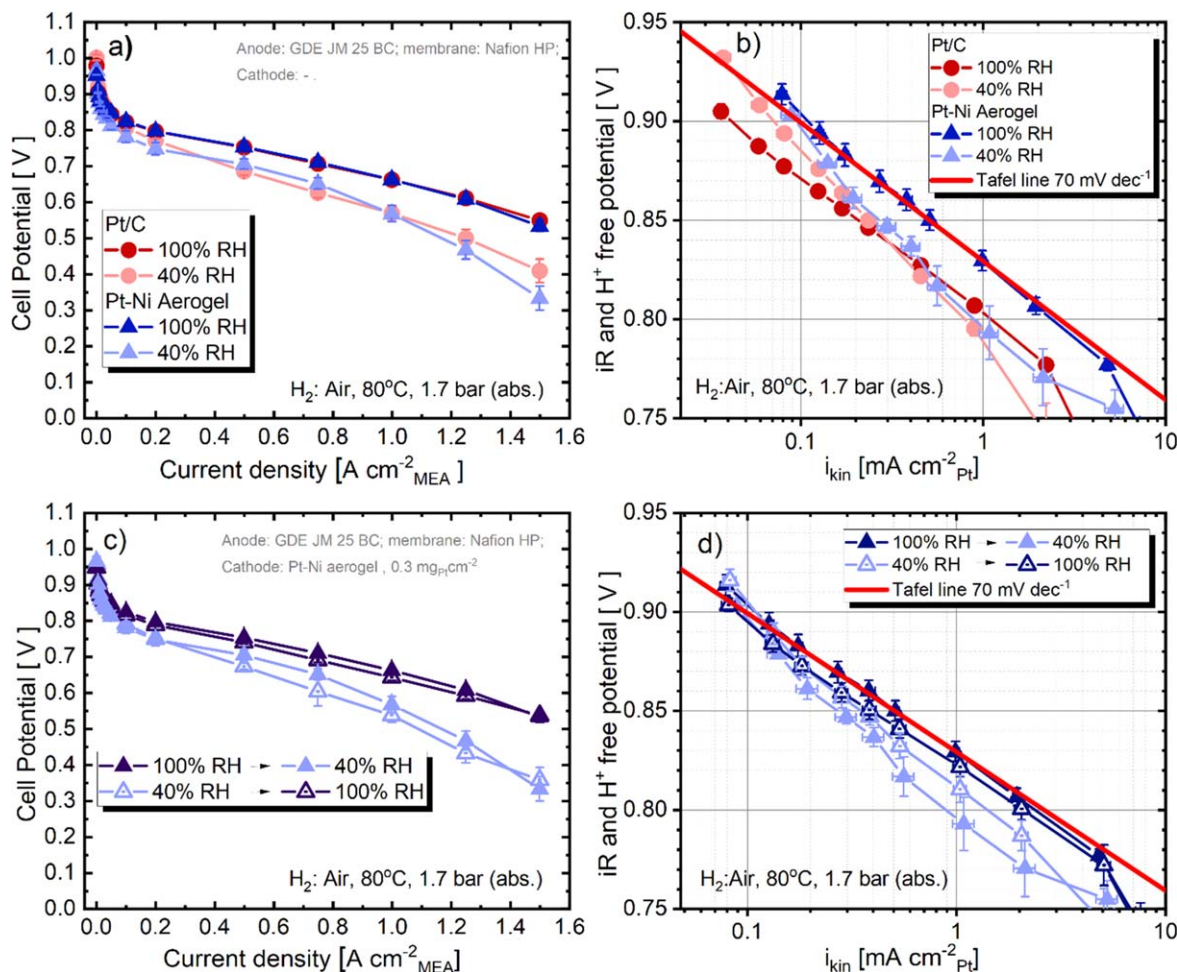


**Figure 1.** Polarization curves recorded on Pt/C and Pt-Ni aerogel CLs in  $\text{H}_2$ :air at  $80^\circ\text{C}$  and 1.70 bar<sub>abs</sub>, and corresponding Tafel plots (b), in both cases as derived from the measurements going from 100 to 40% relative humidity (i.e., in the RH\_1 mode in Table 1). Comparison of the polarization curves recorded by going from 100 to 40 vs 40 to 100% RH (i.e., in RH\_1 vs RH\_2 modes, respectively – (c) and corresponding Tafel plots (d) for Pt-Ni aerogel CLs. Note that in all cases the Pt-loadings are 0.3 vs  $0.4 \text{ mg}_{\text{Pt}}\text{cm}^{-2}$  for the Pt-Ni aerogel vs Pt/C CLs, and that error bars represent the absolute deviation of three independent MEA measurements.

humidification extents. Beyond these catalyst- and RH-specific differences among  $R_{\text{H}^+, \text{cathode}}$  values, the HFRs determined at the various RHs applied in these measurements are essentially identical for both sorts of CLs (see Fig. S2). This lack of sensitivity to the catalysts' nature should be expected, though, since the HFR is dominated by resistances to the transport of protons through the membrane and of electrons at the bipolar plate/GDL as well as CCL/GDL contact points, and these components and interfaces remain the same for the tests performed with Pt/C and the Pt-Ni aerogel as shown in Fig. S9 of the supplementary information.

Finally, the remaining mass transport overpotential is displayed in Fig. 2c, which shows that at  $80^\circ\text{C}$  and 100% RH the Pt-Ni aerogel and Pt/C CLs possess comparable mass transport overpotentials of  $\approx 70 \text{ mV}$  and  $\approx 60 \text{ mV}$ , respectively. These values remain constant for both materials and in both RH-measurement modes (within the standard deviations intrinsic to such measurements) when the RH is progressively decreased down to 60%. However, when further lowering the relative humidity down to 40% RH, a comparable and significant increase of the mass transport resistance is observed for both Pt/C and Pt-Ni aerogel CLs.

This enhancement of the mass transport overpotential at low RHs may appear surprising since, in general, low humidifications favor a reduction of the water content in the GDL and CL that should translate into an improvement in the diffusion of the gas through the cathode.<sup>30</sup> However, this behavior is highly dependent on the flow

field configuration, as explained by Oberholzer et al.<sup>31</sup> using (among others) the specific flow field configuration featured by the differential cell used in this work. Specifically, this cell design uses channels and ribs with the same width, which leads to significant channel-to-rib inhomogeneities in the distribution of the current density<sup>32</sup> and relative humidity that in turn create a longer thermal path and result in a higher temperature along the channel than in the rib.<sup>31</sup> As a result of this, in dry conditions this cell configuration is known to exhibit the increase in bulk diffusion losses observed here at RHs  $< 60\%$ , and that is attributed to resistances to the above inhomogeneities in current-, RH- and temperature-distribution, as well as losses associated to the lateral diffusion of oxygen throughout the GDL.

**Cause of the ORR-activity variation with relative humidity.**—As showcased in the above Figs. 1b, 1d and 2a, the Pt-Ni aerogel suffered from a decrease of the surface-specific ORR-activity as the relative humidity is lowered, while for Pt/C the ORR-kinetic performance stayed unchanged at all RHs. On top of this, Fig. 1b unveils that at 40% RH both materials feature a Tafel slope (TS) that significantly diverges from the  $\approx 70 \text{ mV}\cdot\text{dec}^{-1}$  typically observed under fully humidified conditions and at  $80^\circ\text{C}$ .<sup>15,16</sup> Many studies have tried to explain this RH-dependency of the Tafel slope and its impact on the ORR kinetics,<sup>24,33,34</sup> which is generally ascribed to the potential-dependent presence of ORR-inactive surface Pt-oxides. Thus, to determine the reason for the poorer kinetic performance

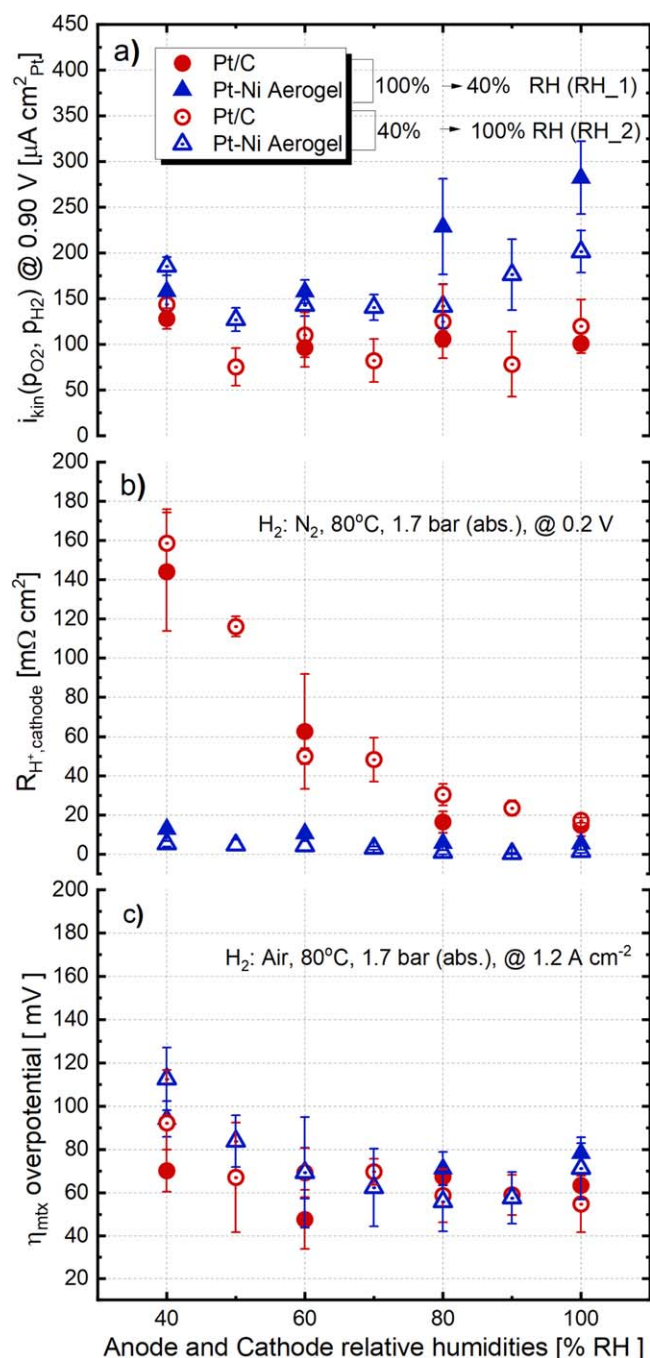


**Figure 2.** Effect of the relative humidity on the Pt-surface-specific ORR-activity values at 0.9 V of Pt/C and Pt-Ni aerogel CLs derived from the Tafel plots in Fig. 1b (a). Corresponding RH-effect on the values of  $R_{H^+,cathode}$  of each material derived from  $H_2:N_2$  PEIS measurements at 0.2 V (b). Mass transport overpotential ( $\eta_{mtx}$ ) at 1.2 A  $cm^{-2}$ , derived as the difference between the measured potential and the extrapolated Tafel line (HFR- and  $R_{H^+,cathode}$ -corrected) at the same current density. Error bars represent standard deviations of the reported, average values based on three independent MEAs measurements.

displayed by the Pt-Ni aerogel at low RHs, in what follows we performed a qualitative Pt-oxide coverage study.

To determine the Pt-oxide coverage we restored to the CVs recorded with  $N_2$  at the cathode and at 100 or 40% RH (displayed in Fig. 3a vs S8 for the Pt-Ni aerogel and Pt/C, respectively), and divide the charge under the Pt-oxide formation or reduction region at potentials  $>0.5$  V ( $Q_{Pt-oxide}$ ) by the whole charge under the H-ad-/

de-sorption region  $<0.4$  V ( $Q_{H-ad-/de-sorption}$ ). In doing so, we assume that the Pt-oxide formation reaction entails a one electron transfer per surface Pt atom, according to the reaction:<sup>25</sup>



On this basis, the CVs and corresponding Pt-oxide coverages in Figs. 3 and S8 feature smaller coverage values at any given potential in the voltammograms recorded at 40% RH as compared to those at full humidification, in good qualitative agreement with what has been previously reported for Pt/C electrodes.<sup>17</sup> To allow for a clear comparison among both catalysts, Fig. 3c showcases the Pt-oxide coverages featured by the Pt-Ni aerogel and Pt/C at the potential of 0.9 V typically used to assess ORR-kinetics and at 100 or 40% RH. In a subsequent step, one can attempt to qualitatively account for these RH-dependent ORR-activity differences by assuming that the corresponding kinetic currents at 0.9 V ( $i_{kin,0.9V}(RH)$ ) can be regarded as being proportional to the product of (i) an “intrinsic” and coverage-independent kinetic current ( $i_{kin,0.9V,intrinsic}$ ), and (ii) the corresponding fraction of non-oxidized surface sites available to catalyze the ORR, according to the expression:

$$i_{kin,0.9V}(RH) \propto i_{kin,0.9V,intrinsic} \cdot [1 - \theta_{PtOx,0.9V}(RH)] \quad [7]$$

where  $\theta_{PtOx,0.9V}(RH)$  is the Pt-oxide coverage at 0.9 V and the given relative humidity. On this basis, and looking first at the results at fully humidified conditions, the Pt-oxide coverages at 0.9 V ( $\theta_{PtOx,0.9V}^{100\%RH}$ ) in Fig. 3c are significantly higher for the Pt-Ni aerogel vs Pt/C (with values of  $\approx 0.85$  vs  $\approx 0.55$ , respectively, as averaged from the positive- and negative-going potential scans). Considering the surface-specific ORR-activity values at the same potential and 100% RH in Fig. 2a ( $\approx 250$  vs  $\approx 100 \mu A \cdot cm_{Pt}^{-2}$ ), the corresponding intrinsic activity values derived from Eq. 4 would account to  $\approx 1670$  vs  $\approx 220 \mu A \cdot cm_{Pt}^{-2}$  for the Pt-Ni aerogel vs Pt/C, respectively. In other words, when accounting for the actual number of catalytically-available (i.e., non-oxidized) surface sites through this simplified approach, those in the Pt-Ni aerogel would feature an intrinsic ORR-activity (directly tied to their turn-over frequency)  $\approx 7.5$ -fold greater than those in the non-alloyed, Pt/C catalyst.

Conversely, at 40% RH, the corresponding  $\theta_{PtOx,0.9V}^{40\%RH}$  values are  $\approx 0.30$  vs  $\approx 0.75$  for Pt/C vs Pt-Ni aerogel (cf Fig. 3c), respectively, which in combination with the intrinsic activities reported above would result in  $i_{kin,0.9V}$  (40%) values of  $\approx 150$  vs  $\approx 410 \mu A \cdot cm_{Pt}^{-2}$  for each of these materials. Whereas the former value agrees well with the performance of the Pt/C CL at 40% RH in Fig. 2a, in the aerogel's case the predicted value is  $\approx 2$ -fold higher than what was experimentally determined and plotted in the same figure. Thus, a more detailed and fully quantitative kinetic study taking into careful consideration these coverage-dependent effects<sup>24,35</sup> is needed in order to account for these performance differences, and will be the subject of our next publication.

**Temperature effect.**—The effect of temperature on the Pt/C and Pt-Ni aerogel CLs' performance is showcased in the polarization curves at the most extreme temperatures of 40 and 80 °C displayed in Fig. 4a (with all other curves presented in Fig. S10). Both CL-sorts feature a poorer performance with decreasing temperature, as one may expect based on the decrease of the gas diffusivity and membrane conductivity at lower temperatures.<sup>34,36,37</sup> Moreover, such low temperatures can enhance the chances for water condensation, which can in turn lead to the flooding of the cathode catalyst layer. This appears to be the case for the Pt-Ni aerogel, since in the test at 40 °C and at the highest tested current of 1.5 A  $cm^{-2}$  the measured potential was systematically  $<0$  V (and thus this point is not included in the polarization curve in Fig. 4a).

One of the main kinetic parameters that can be inferred from such a temperature variation study is the activation energy of the ORR on the catalyst's surface as described by the equation:<sup>22</sup>



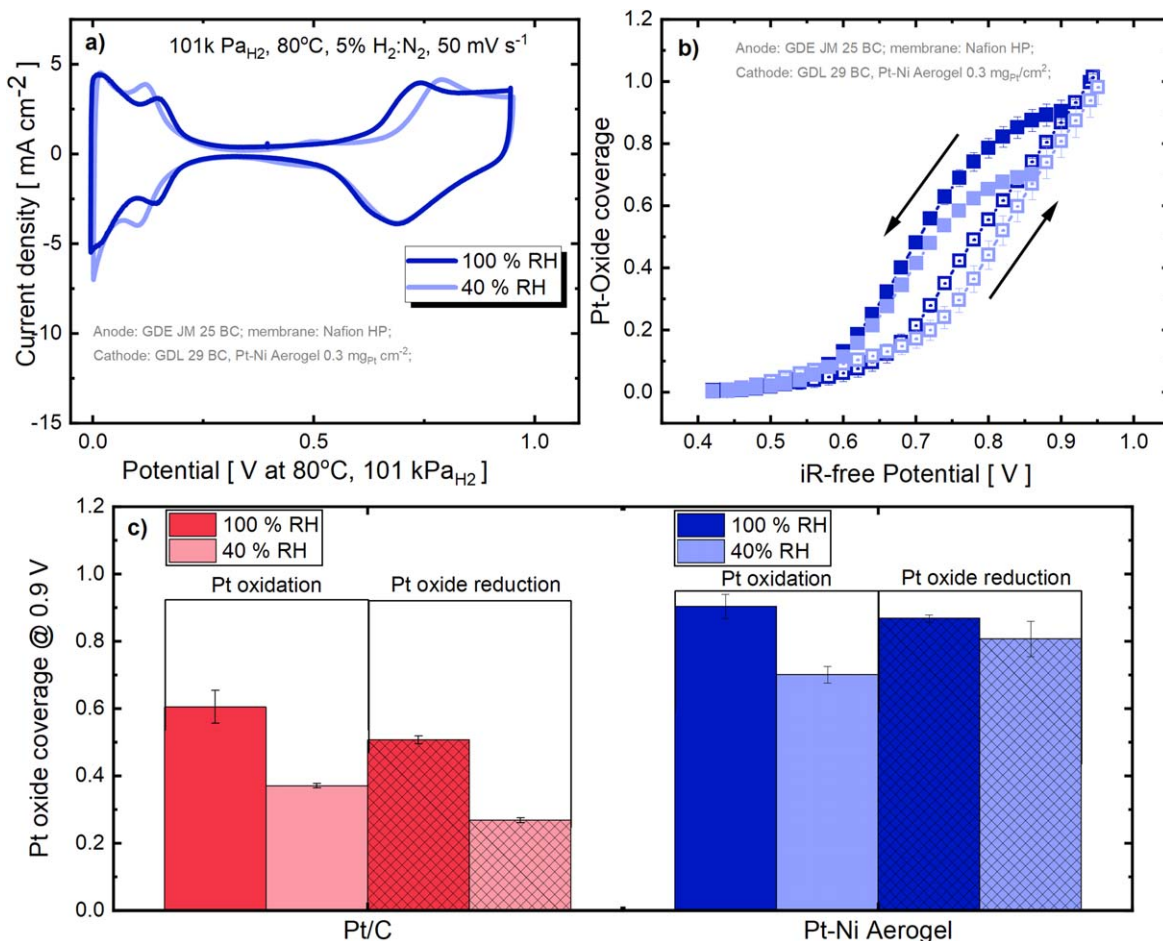


**Figure 3.** Cyclic voltammograms recorded on the Pt-Ni aerogel cathode CL using 5% H<sub>2</sub> in argon on the anode and with the N<sub>2</sub> flow stopped at the cathode, at 80 °C, 1.70 bar<sub>abs</sub> and 100 or 40% RH. Note that the potential is iR- corrected and referenced to a standard H<sub>2</sub> pressure of 1.01 bar (a). Corresponding potential-dependent Pt-oxide coverages obtained by integrating the anodic or cathodic CV scans (filled vs empty symbols, respectively) and dividing them by the overall hydrogen underpotential deposition charge (b). Bar plots comparing the Pt-oxide coverage values at 0.9 V at 100 or 40% RH and for Pt/C or Pt-Ni aerogel CLs (c).

$$2.303R \left. \frac{\partial \log i}{\partial 1/T} \right|_{\eta, p_{O_2}} = E_{act} \quad [8]$$

Thus, the activation energies were calculated from the relation between the inverse of the temperature and the logarithm of the corresponding current densities at an overpotential of 350 mV (in which all considered currents remain within the Tafel regime), which were previously H<sub>2</sub>-crossover corrected and referenced to an O<sub>2</sub> pressure ( $p_{O_2}^*$ ) of 1.01 bar<sub>abs</sub> using the equation

$$i_{p(O_2)}|_{\eta, T, p_{H_2}} = i_{Air} \cdot \left( \frac{p_{O_2}}{p_{O_2}^*} \right)^\gamma \quad [9]$$

where  $\gamma$  is the reaction order with respect to the O<sub>2</sub>-pressure and at constant overpotential, with an assumed value of 0.54.<sup>22</sup> The corresponding log(*i*) vs 1/*T* plots are featured in Fig. 4b, and the derived activation energy values for the two materials and as function of the data acquisition protocol are listed in Table IV. The latter unveils that when the temperature variation tests were performed in the T<sub>1</sub> mode (i.e., going from high to low temperatures), both the Pt/C and Pt-Ni aerogel CLs feature a similar activation energy of  $\approx 30$  kJ·mol<sup>-1</sup> that is also consistent with the 33 kJ·mol<sup>-1</sup> reported by Neyerlin et al. for a Pt/C CL. This observation is consistent with that of Seel et al.,<sup>38</sup> who compared high-temperature fuel cell (HT-PEFC) measurements on Pt/Ni/C with

what was reported by Neyerlin et al.<sup>22</sup> in a low temperature PEFC, respectively. Specifically, the authors confirmed that the activation energies of the Pt/C and Pt-alloys are comparable, and that only the exchange current densities of these materials are significantly different. Moreover, this similarity between the catalysts' activation energies is also observed when considering the data acquired in the T<sub>2</sub> mode, which appears to yield a  $\approx 30\%$  higher  $E_{act}$  value of  $\approx 40$  kJ·mol<sup>-1</sup> that on the other hand remains consistent with the T<sub>1</sub> mode value when considering the error bars associated to these parameters.

Moving on to the effect of the temperature on  $R_{H+cathode}$  (see Fig. 4c, in the same way as what was observed above for the impact of RH on this variable for the Pt-Ni aerogel CLs, their reduced thickness entail negligible proton transport resistances that are barely modified upon decreasing the temperature to 40 °C. However, for the Pt/C CL this proton resistance increases  $\approx 2$ -fold when lowering the temperature from 80 °C to 40 °C, in good agreement with the halving of the proton conductivity reported for a perfluorosulfonic acid membrane submitted to the same temperature decrease.<sup>39</sup>

Finally, the mass transport overpotential values at 1.2 A·cm<sup>-2</sup> for both materials are displayed in Fig. 4d, which shows that as the temperature is decreased <80 °C, the  $\eta_{mtx}$  values of the aerogel CLs become increasingly larger than those of Pt/C. We hypothesize that this difference among materials stems from the reduced thickness and lack of hydrophobicity of the aerogel CL, which translates into insufficient void volume to store and evacuate the water that

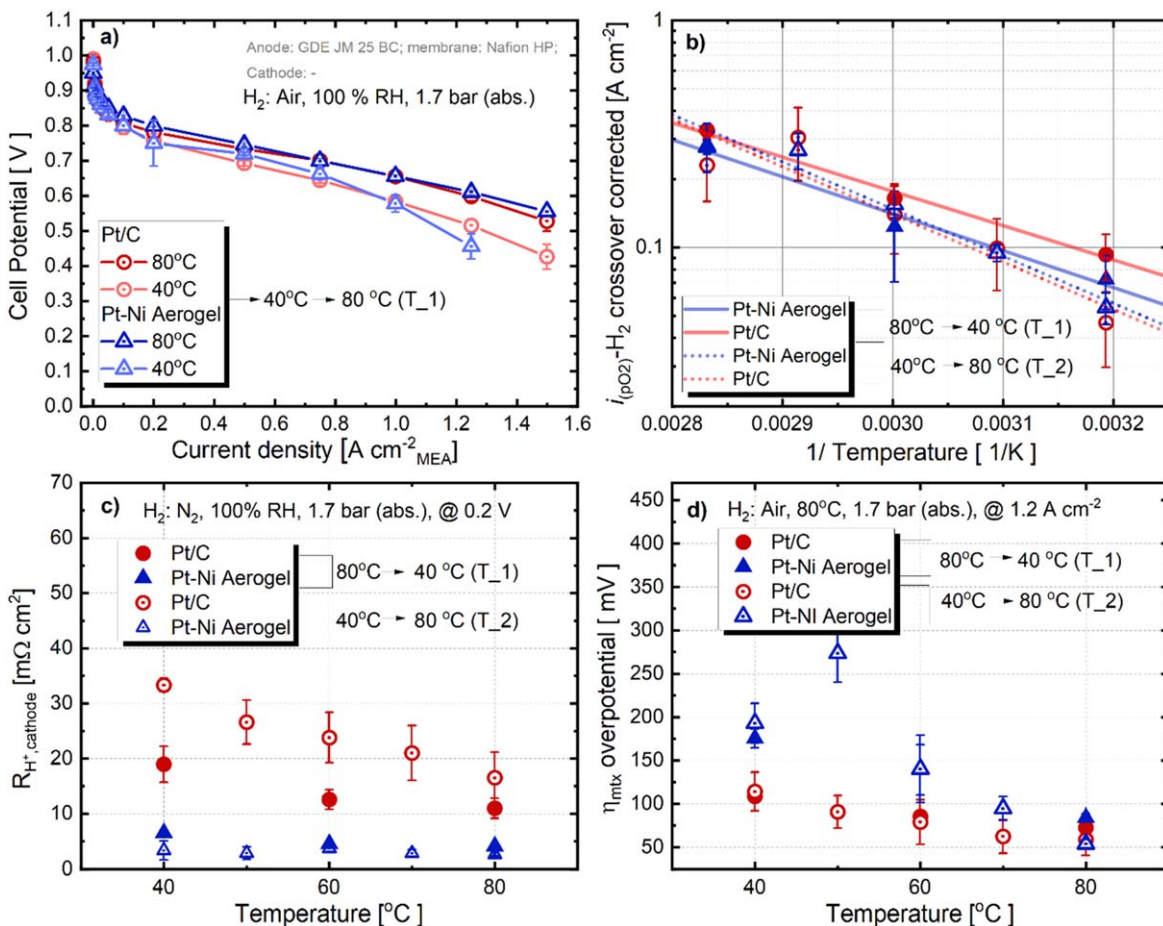


**Figure 4.** Polarization curves recorded on Pt/C and Pt-Ni aerogel CLs using the  $T_2$  protocol in Table II, in which the relative humidity is maintained at 100% and the temperature of the cell is increased from 40 to 80  $^{\circ}\text{C}$ , with 600  $\text{nmL min}^{-1}$  of  $\text{H}_2$  in the anode and 1350  $\text{nmL min}^{-1}$  of air in the cathode (a). Arrhenius plot featuring the logarithmic of the current density (corrected to a reference  $\text{H}_2$  pressure of 1.01 bar) and at a constant overpotential of 350 mV (see Eq. 8 below) vs the reciprocal of the cell temperature (b). Temperature dependency of the proton resistance through the cathode CL ( $R_{\text{H}^+, \text{cathode}}$ ) derived from the impedance spectra recorded at 0.2 V in  $\text{H}_2$ :  $\text{N}_2$  at 100% RH and various temperature (c). Corresponding mass transport overpotentials as a function of temperature, for a current of 1.2  $\text{A cm}^{-2}$ .

**Table IV. Activation energies determined at a constant overpotential of 350 mV and a reference  $\text{O}_2$  pressure ( $p_{\text{O}_2}^*$ ) of 1.01 bar $_{\text{abs}}$ .**

Experiment order	Catalyst	$E_{\text{act}}$ at $\eta = 0.35$ V [ $\text{kJ mol}^{-1}$ ]
$T_1$	Pt/C <sup>22</sup>	33
	Pt/C	$29 \pm 3$
	Pt-Ni Aerogel	$31 \pm 5$
$T_2$	Pt/C	$39 \pm 4$
	Pt-Ni Aerogel	$40 \pm 8$

condensed at such lower operative temperatures. Notably, this difference among materials maxes out at 50  $^{\circ}\text{C}$  but then slightly decreases at 40  $^{\circ}\text{C}$  (at which the aerogel features  $\approx 3$ - vs  $\approx 2$ -fold larger  $\eta_{\text{mtx}}$ -values than Pt/C). While the reason for this behavior is still unknown, it might be indicative of temperature inhomogeneities caused by limitation in the rejection of heat at these high current densities (since the cells used for these measurements are devoid of active cooling), and that would therefore be more relevant for the tests performed at the lower nominal temperature of 40  $^{\circ}\text{C}$ .

**Up-transient tests.**—To finalize this work, Fig. 5 shows the minimum voltages responses obtained in the current up-transient tests at various RHs (Fig. 5a) and temperatures (Fig. 5b) for both Pt/C and Pt-Ni aerogel CLs. These measurements were performed in

both the RH\_1 and RH\_2 and  $T_1$  and  $T_2$  modes, which in all cases led to fully comparable results that discard an impact of this measurement mode on the observed behaviors. Interestingly, all electrodes (including those of the Pt-Ni aerogel) featured a minimum voltage  $> 0$  V at all RH conditions, suggesting that the void volume in the aerogel CL is sufficient to store and remove the water instantaneously generated at this high current density even under high humidifications maximizing the chances for water condensation. This observation ties in with the work of Kongkanand et al.<sup>19</sup> on nanostructured thin films (NSTFs)<sup>40,41</sup> that, due to their unsupported nature, also result in ultra-thin CLs ( $\approx 0.3 \mu\text{m}$ ), and that suffered from flooding and led to cell failure when submitted to the same up-transient tests at 90 or 100% RH. Notably, our Pt-Ni aerogel CLs remain  $\approx 5$ -fold thicker than the NSTFs, and are therefore comparable to a  $\approx 1 \mu\text{m}$  thick Pt/CL featured in the same study by Kongkanand and coworkers,<sup>19</sup> and that also featured a minimum potential  $> 0$  V in these transient tests at high humidifications.

In addition, these current ramp-up experiments were also performed at temperatures  $\leq 80$   $^{\circ}\text{C}$  to evaluate the possible effect of water condensation (more likely at lower temperatures) on the response of both materials' CLs. As shown in Fig. 5b, the Pt/C and Pt-Ni aerogel layers show comparable minimum voltages in all tests at temperatures  $\geq 60$   $^{\circ}\text{C}$ . However, when decreasing the temperature down to 40  $^{\circ}\text{C}$ , the aerogel CLs feature a minimum voltages significantly lower than those of the Pt/C layers at the same conditions ( $\approx 0.45$  vs  $\approx 0.65$  V for Pt-Ni aerogel vs Pt/C,



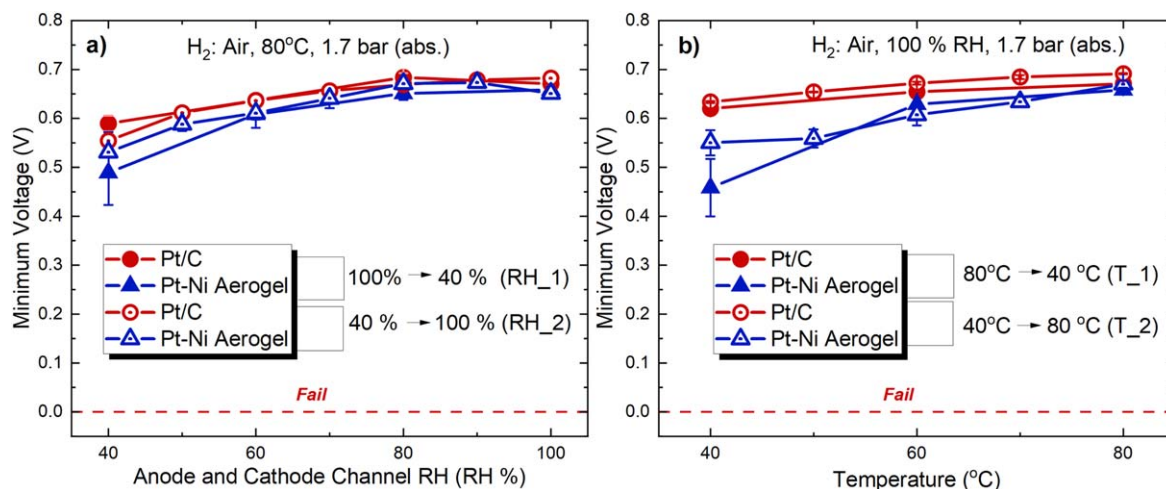


**Figure 5.** Minimum cell voltages in current up-transient experiments going from 0.02 to 1 A·cm<sup>-2</sup> in 1 s at various RHs and a cell temperature of 80 °C (a) or at different temperatures and a fixed RH of 100% (b). All tests were performed at 1.70 bar<sub>abs</sub> and with H<sub>2</sub> and air fed to the anode vs cathode, respectively.

respectively), indicating that at even lower temperatures the condensation of water may lead to the flooding of the aerogel CLs.

### Conclusions

In the present contribution we studied the effect of automotive-relevant conditions (i.e., temperatures <80 °C, relative humidities <100% and fast current up-transients) on performance of Pt-Ni aerogel cathode CLs, which was systematically benchmarked against a commercial Pt/C cathode. Our results at high vs low RHs show that, unlike Pt/C, the Pt-Ni aerogel suffers a decrease of its ORR-kinetic performance at low humidifications that can be partially ascribed to the larger Pt-oxide coverage displayed by this material (vs Pt/C) under such conditions. Complementarily, in these tests at different RHs both materials feature resembling mass transport overpotentials that increase under dry conditions, possibly because the cell design causes inhomogeneities in temperature and current distribution along the channels and ribs. Moreover, the aerogel CL shows a significant lower proton transport resistance than Pt/C at low relative humidity, but this performance advantage at low RHs is compensated by the lower kinetic performance under equivalent conditions discussed above.

As for the tests at temperatures <80 °C, at the most extreme tested condition of 40 °C and the highest current of 1.5 A·cm<sup>-2</sup> the aerogel showed a poorer performance than Pt/C, possibly due to the flooding of its thin catalyst layer with water. This behavior was partially reproduced in the up-transient experiments to 1 A·cm<sup>-2</sup> at 40 °C, in which the aerogel CL's voltage response was sufficient to pass the test but led to a minimum voltage remarkably low when compared to Pt/C.

In summary, this study highlights the challenges that Pt-Ni aerogel CLs can face for their implementation in realistic automotive conditions. The knowledge acquired through this comparison with a commercial Pt/C material will be used to guide the optimization of aerogel CLs<sup>41,42</sup> and/or to tune the operating conditions encountered by such thin catalyst layers.

### Acknowledgments

The authors gratefully acknowledge funding from the Swiss National Science Foundation under the funding scheme Sinergia (project grant number 180335) and the Deutsche Forschungsgemeinschaft (DFG EY 16/30-1). The authors would like to also thank Mr. Álvaro García-Padilla for his help programming a code to quantify the Pt-hydroxide coverage values. Furthermore, we are grateful to Dr. Pierre Boillat for the fruitful discussions regarding the interpretation of the low relative humidity results.

### ORCID

Meriem Fikry <https://orcid.org/0000-0002-1352-6947>

Juan Herranz <https://orcid.org/0000-0002-5805-6192>

### References

- S. T. Thompson and D. Papageorgopoulos, *Nat. Catal.*, **2**, 558 (2019).
- A. Rabis, P. Rodriguez, and T. J. Schmidt, *ACS Catal.*, **2**, 864 (2012).
- S. Henning, R. Shimizu, J. Herranz, L. Kühn, A. Eychmüller, M. Uchida, K. Kakimura, and T. J. Schmidt, *J. Electrochem. Soc.*, **165**, F3001 (2018).
- S. Henning, J. Herranz, H. Ishikawa, B. J. Kim, D. Abbott, L. Kühn, A. Eychmüller, and T. J. Schmidt, *J. Electrochem. Soc.*, **164**, F1136 (2017).
- L. Castanheira, W. O. Silva, F. H. B. Lima, A. Crisci, L. Dubau, and F. Maillard, *ACS Catal.*, **5**, 2184 (2015).
- Y. Wang, B. Seo, B. Wang, N. Zamel, K. Jiao, and X. C. Adroher, *Energy AI*, **1**, 100014 (2020).
- "DOE Technical Targets for Polymer Electrolyte Membrane Fuel Cell Components," can be found under (<https://energy.gov/eere/fuelcells/doe-technical-targets-polymer-electrolyte-membrane-fuel-cell-components>). Accessed on 01.08.2023.
- S. Henning, H. Ishikawa, L. Kühn, J. Herranz, E. Müller, A. Eychmüller, and T. J. Schmidt, *Angew. Chem.*, **129**, 10847 (2017).
- M. Fikry, N. Weiss, M. Bozzetti, S. Ünsal, M. Georgi, P. Khavlyuk, J. Herranz, V. Tileli, A. Eychmüller, and T. J. Schmidt, *Submitt. ACS Appl. Energy Mater.*, n.d.
- M. Povia, J. Herranz, T. Binnering, M. Nachttegaal, A. Diaz, J. Kohlbrecher, D. F. Abbott, B.-J. Kim, and T. J. Schmidt, *ACS Catal.*, **8**, 7000 (2018).
- P. Oberholzer and P. Boillat, *J. Electrochem. Soc.*, **161**, F139 (2013).
- P. Oberholzer, P. Boillat, R. Siegrist, A. Kästner, E. H. Lehmann, G. G. Scherer, and A. Wokaun, *Electrochem. Commun.*, **161**, 67 (2012).
- J. N. Schwämmlein, P. J. Rheinländer, Y. Chen, K. T. Freyer, and H. A. Gasteiger, *J. Electrochem. Soc.*, **165**, F1312 (2018).
- V. K. Ramani, K. Cooper, J. M. Fenton, and H. R. Kunz, *Springer Handb. Electrochem. Energy*, ed. C. Breitkopf and K. Swider-Lyons (Springer, Berlin, Heidelberg) p. 649 (2017).
- H. A. Gasteiger, S. S. Kocha, B. Sompalli, and F. T. Wagner, *Appl. Catal. B Environ.*, **56**, 9 (2005).
- K. C. Neyerlin, W. Gu, J. Jorne, A. Clark, and H. A. Gasteiger, *J. Electrochem. Soc.*, **154**, B279 (2007).
- Y. Liu, M. W. Murphy, D. R. Baker, W. Gu, C. Ji, J. Jorne, and H. A. Gasteiger, *J. Electrochem. Soc.*, **156**, B970 (2009).
- R. Makharia, M. F. Mathias, and D. R. Baker, *J. Electrochem. Soc.*, **152**, A970 (2005).
- A. Kongkanand and P. K. Sinha, *J. Electrochem. Soc.*, **158**, B703 (2011).
- K. C. Neyerlin, W. Gu, J. Jorne, and H. A. Gasteiger, *J. Electrochem. Soc.*, **154**, B631 (2007).
- D. M. Bernardi and M. W. Verbrugge, *J. Electrochem. Soc.*, **139**, 2477 (1992).
- K. C. Neyerlin, W. Gu, J. Jorne, and H. A. Gasteiger, *J. Electrochem. Soc.*, **153**, A1955 (2006).
- R. N. Carter, S. S. Kocha, F. Wagner, M. Fay, H. A. Gasteiger, and E. C. S. Trans, *J. Electrochem. Soc.*, **11**, 403 (2007).
- N. P. Subramanian, T. A. Greszler, J. Zhang, W. Gu, and R. Makharia, *J. Electrochem. Soc.*, **159**, B531 (2012).
- H. Angerstein-Kozłowska, B. E. Conway, and W. B. A. Sharp, *J. Electroanal. Chem. Interfacial Electrochem.*, **43**, 9 (1973).
- R. Chattot et al., *Nat. Mater.*, **17**, 827 (2018).
- R. Chattot, I. Martens, M. Scohy, J. Herranz, J. Drnec, F. Maillard, and L. Dubau, *ACS Energy Lett.*, **5**, 162 (2020).

28. H. Kuroki, Y. Imura, R. Fujita, T. Tamaki, and T. Yamaguchi, *ECS Meet. Abstr.*, **MA2020-02**, 2316 (2020).
29. H. Kuroki, Y. Imura, R. Fujita, T. Tamaki, and T. Yamaguchi, *ACS Appl. Nano Mater.*, **3**, 9912 (2020).
30. Q. Yan, H. Toghiani, and J. Wu, *J. Power Sources*, **158**, 316 (2006).
31. P. Oberholzer, P. Boillat, A. Kaestner, E. H. Lehmann, G. G. Scherer, T. J. Schmidt, and A. Wokaun, *J. Electrochem. Soc.*, **160**, F659 (2013).
32. I. A. Schneider, M. H. Bayer, and S. von Dahlen, *J. Electrochem. Soc.*, **158**, B343 (2011).
33. Y. Liu, M. Mathias, and J. Zhang, *Electrochem. Solid-State Lett.*, **13**, B1 (2009).
34. H. Xu, Y. Song, H. R. Kunz, and J. M. Fenton, *J. Electrochem. Soc.*, **152**, A1828 (2005).
35. S. Gottesfeld, *J. Electrochem. Soc.*, **169**, 124518 (2023).
36. Q. Yan, H. Toghiani, and H. Causey, *J. Power Sources*, **161**, 492 (2006).
37. J. Zhang, H. Zhang, J. Wu, and J. Zhang, in *Pem Fuel Cell Test. Diagn.*, ed. J. Zhang, H. Zhang, J. Wu, and J. Zhang (Elsevier, Amsterdam)p. 121 (2013).
38. D. C. Seel, B. C. Benicewicz, L. Xiao, and T. J. Schmidt, *Handb. Fuel Cells* (John Wiley & Sons, Ltd) (2010).
39. C. K. Mittelsteadt and H. Liu, *Handb. Fuel Cells* (John Wiley & Sons, Ltd) (2010).
40. P. K. Sinha, W. Gu, A. Kongkanand, and E. Thompson, *J. Electrochem. Soc.*, **158**, B831 (2011).
41. A. Kongkanand, J. E. Owejan, S. Moose, M. Dioguardi, M. Biradar, and R. Makharia, *J. Electrochem. Soc.*, **159**, F676 (2012).
42. A. Kongkanand, M. Dioguardi, C. Ji, and E. L. Thompson, *J. Electrochem. Soc.*, **159**, F405 (2012).